Transient Stability Analysis of a Hybrid Offshore Wind Farm Connected to a Hybrid HVDC Link with a Supercapacitor-based Energy Storage System and a High Temperature Superconducting Coil

Li Wang, Ting-Wei Hong, and Ching-Chung Tseng
Department of Electrical Engineering
National Cheng Kung University
Tainan City 701401, Taiwan
liwang@mail.ncku.edu.tw

Aji Akbar Firdaus
Department of Engineering, Faculty of Vocational
Universitas Airlangga
Surabaya, Indonesia
aa.firdaus@vokasi.unair.ac.id

***Abstract*—This paper presents the transient stability analysis of integrating a superconducting synchronous generator (SCSG)-based offshore wind farm (OWF) and a permanent-magnet synchronous generator (PMSG)-based OWF fed to the simplified Taiwan Power System through a hybrid high-voltage direct current (HVDC) link. The DC line of the hybrid HVDC link has a supercapacitor (SC)-based energy storage system (ESS) and a high-temperature superconducting coil (HTSCC). The hybrid HVDC link has two AC/DC voltage source converters (VSCs) connected to the two OWFs and a line-commutated converter (LCC)-based DC/AC inverter connected to the simplified Taiwan Power System. The comparative transient stability of the studied system with and without the SCESS and the designed lead-lag damping controller for the LCC inverter of the HVDC link is performed. The simulation results show that the LCC-based inverter with the designed lead-lag damping controller can suppress the transient characteristics of the studied system under severe disturbance conditions.**

***Index Terms*--Superconducting synchronous generator, permanent-magnet synchronous generator, high-voltage direct-current link, supercapacitor, high-temperature superconducting coil, stability.**

I. Introduction

Since the development of the traditional and high-technology industry, fossil fuels have been widely used. However, consuming fossil fuels produces large amounts of carbon dioxide, and it can cause the greenhouse effect and lead to significantly abnormal climate phenomena. Therefore, the research and development of renewable energy has begun to receive more attention, and wind energy is one of the fastest-growing renewable energy resources (RERs) in the world. Due to the changes of the seasons, climate, and wind speed, wind energy is an unpredictable RER. When large-scale OWFs are connected to a power system, the instantaneous change in wind speed can harm the power system, thus causing severe damage to the power quality and stability of the power system. Since an HVDC link can integrate various RERs and transmit bulk electricity power through long-distance cables, it can make the voltage of a wind power system become more stable and control the power flow by using power-electronics converters when the connected power system is under disturbance.

The HTSCC used in an HVDC link as an energy buffer can smooth wind power fluctuations, and the HVDC link can take advantage for system stability improvement [1]-[2]. Since the SCs have high power density and long cycle life [3], an SC-based ESS can improve the voltage variations of wind power and regulate the power of the power system.

This paper is organized as follows. Section II introduces system configuration and employed models. The design procedure and design results for the damping controller of the LCC-based inverter in the hybrid HVDC link using the phase-compensation method are depicted in Section III. Section IV presents the transient responses of the studied system. Finally, the specific conclusions of this paper are drawn in Section V.

II. System Architecture and Employed Mathematical Models

A. System Architecture

Fig. 1 shows the integration of an SCSG-based OWF of 100 MW and a PMSG-based OWF of 60 MW fed to the simplified Taiwan Power System through a 200-MW hybrid HVDC link, where the HVDC line includes an SCESS of 50 MW and an HTSCC. The simplified Taiwan Power System includes four large-scale equivalent synchronous generators (SGs), G1-G4, which are connected to the buses of Nuclear 2 #G, Hsie-Ho #G, Chung-Ho #G, and Hsin-Ta #G, respectively [4]-[6]. The 2030 off-peak power flow data of the Taiwan Power System are carefully selected as a simulation basis.

979-8-3315-8138-1

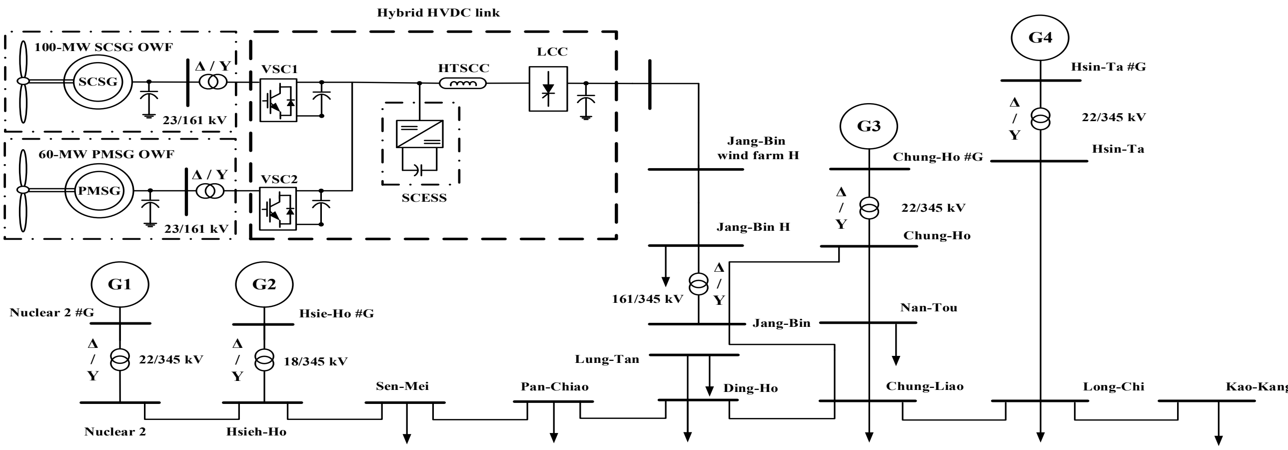

Figure 1. Configuration of the studied system.

B. Model of Wind Turbine

The mechanical power extracted by a typical variable-speed wind turbine (VSWT) can be expressed by [7]

$$P_w = (0.5)\cdot \rho \cdot \pi \cdot R_B^2 \cdot V_W^3 \cdot C_p(\lambda, \beta) \tag{1}$$

where ρ is the air density (kg/m^3), R_t is the blade length (m), V_w is the wind speed (m/s), and $C_p(\lambda, \beta)$ is the power coefficient of the VSWT. The value of $C_p(\lambda, \beta)$ is a function of the tip speed ratio λ ($\lambda = R_B\omega_B/V_w$) and the blade pitch angle β (degrees). A two-inertia reduced-order equivalent mass-spring-damper model can represent the dynamics of a VSWT coupled to the rotor of a wind generator.

C. Wind SCSG Model

The per-unit q-d axis voltage-current differential equations of a wind SCSG are given by [8]-[10]

$$v_{qSC} = (-r_{sSC} - \frac{p}{\omega_b}X_{qsSC})i_{qSC} - (\frac{1}{\omega_b}\omega_{rSC}X_{dsSC})i_{dSC} + (\frac{1}{\omega_b}\omega_{rSC}X_{mdSC})i_{kdSC} + (\frac{1}{\omega_b}\omega_{rSC}X_{mdSC})i_{fdSC} - (\frac{p}{\omega_b}\omega_{rSC}X_{mqSC})i_{kqSC} \tag{2}$$

$$v_{dSC} = (r_{sSC} - \frac{p}{\omega_b}X_{dsSC})i_{dSC} + (\frac{1}{\omega_b}\omega_{rSC}X_{qsSC})i_{qSC} + (\frac{p}{\omega_b}X_{mdSC})i_{kdSC} + (\frac{p}{\omega_b}X_{mdSC})i_{fdSC} - (\frac{1}{\omega_b}\omega_{rSC}X_{mqSC})i_{kqSC} \tag{3}$$

$$v_{kqSC} = (r_{kqSC} + \frac{p}{\omega_b}X_{qrSC})i_{kqSC} - (\frac{p}{\omega_b}X_{mqSC})i_{qSC} \tag{4}$$

$$v_{kdSC} = (r_{kdSC} + \frac{p}{\omega_b}X_{drSC})i_{kdSC} + (\frac{p}{\omega_b}X_{mdSC})i_{fdSC} - (\frac{p}{\omega_b}X_{mdSC})i_{dSC} \tag{5}$$

$$v_{fSC} = (\frac{p}{\omega_b}X_{mdSC})i_{kdSC} + (r_{fSC} + \frac{p}{\omega_b}X_{fSC})i_{fdSC} - (\frac{p}{\omega_b}X_{mdSC})i_{dSC} \tag{6}$$

where the modulation indices of q-axis and d-axis (m_{qSC} and m_{dSC}) of the system-side converter (SSC) of the SCSG are used to control the maximum power point tracking (MPPT) and the rotational speed of SCSG, respectively. The GSC of the SCSG can control the DC voltage between the SCSG's GSC and SSC, and can make the output power factor unity.

D. Wind PMSG Model

The per-unit q-d axis voltage-current differential equations of a wind PMSG are given by [11-12]

$$v_{qPM} = -r_{sPM}i_{qPM} + p(\lambda_{qPM})/\omega_b + (\omega_{rPM}/\omega_b)(\lambda_{dPM}) \tag{7}$$

$$v_{dPM} = -r_{sPM}i_{dPM} + p(\lambda_{dPM})/\omega_b - (\omega_{rPM}/\omega_b)(\lambda_{qPM}) \tag{8}$$

where

$$\lambda_{qPM} = -(X_{mqPM} + X_{lPM})i_{qPM} \tag{9}$$

$$\lambda_{dPM} = -(X_{mdPM} + X_{lPM})i_{dPM} + X_{mdPM}i_m{}' \tag{10}$$

The modulation indices of q-axis and d-axis (m_{qPM} and m_{dPM}) of the system-side converter (SSC) of the PMSG are used to control the terminal voltage of the wind PMSG and the DC voltage between the PMSG's GSC and SSC, respectively. The GSC of the PMSG can control the rotational speed of the wind PMSG, and can make its output power factor unity.

E. SG Model

The equivalent circuit of the two-axis model is used for the four large-scale SGs of the simplified Taiwan Power System shown in Fig. 1. The control block diagrams of the excitation system (IEEE Type ST1A), the governor model, and the steam turbine torque model of the SGs can be referred to [13].

F. Hybrid HVDC Link Model

The configuration of the hybrid HVDC link is shown in Fig. 1.

1) DC Line. The per-unit voltage-current equations used to simulate the DC line can be obtained directly from Fig. 1.

$$(\frac{C_{Hdc1}}{\omega_b})p(V_{Hdc1}) = i_{dGSC}M_{r1}\sin(\alpha_{r1}+\theta_{b1}) - i_{qGSC}M_{r1}\cos(\alpha_{r1}+\theta_{b1}) - I_{Hdc1} \tag{9}$$

$$(\frac{C_{Hdc2}}{\omega_b})p(V_{Hdc2}) = i_{dGPM}M_{r2}\sin(\alpha_{r2}+\theta_{b2}) - i_{qGPM}M_{r2}\cos(\alpha_{r2}+\theta_{b2}) - I_{Hdc2} \tag{10}$$

$$(\frac{L_{Hdc1}}{\omega_b})p(I_{Hdc1}) = V_{Hdc1} - R_{Hdc1}I_{Hdc1} - V_{DCL} \tag{11}$$

$$(\frac{L_{Hdc2}}{\omega_b})p(I_{Hdc2}) = V_{Hdc2} - R_{Hdc2}I_{Hdc2} - V_{DCL} \tag{12}$$

$$(\frac{C_{DCL}}{\omega_b})p(V_{DCL}) = I_{Hdc1} + I_{Hdc2} - I_{HTSCC} \tag{13}$$

979-8-3315-8138-1

$$(\frac{L_{HTSCC}}{\omega_b})p(I_{HTSCC}) = -\frac{1}{\sqrt{2}}\sqrt{(V_{dINV})^2+(V_{qINV})^2}\cos(\gamma_I) + V_{DCL} + [(\frac{\pi}{6})X_{LCI} - R_{HTSCC}]I_{HTSCC} \quad (14)$$

2) VSCs. The per-unit voltage-current equations used to simulate the OWF's VSC are depicted as follows.

$$(\frac{X_{TS}}{\omega_b})p(i_{qgSC}) = v_{qgSC} - R_{TS}i_{qgSC} - \omega_e X_{TS} i_{dgSC} - V_{Hdc1}M_{r1}\cos(\alpha_{r1}+\theta_{b1}) \quad (15)$$

$$(\frac{X_{TS}}{\omega_b})p(i_{dgSC}) = v_{dgSC} - R_{TS}i_{dgSC} - \omega_e X_{TS} i_{qgSC} - V_{Hdc1}M_{r1}\cos(\alpha_{r1}+\theta_{b1}) \quad (16)$$

$$(\frac{X_{TP}}{\omega_b})p(i_{qgPM}) = v_{qgPM} - R_{TP}i_{qgPM} - \omega_e X_{TP} i_{dgPM} - V_{Hdc2}M_{r2}\cos(\alpha_{r2}+\theta_{b2}) \quad (17)$$

$$(\frac{X_{TP}}{\omega_b})p(i_{dgPM}) = v_{dgPM} - R_{TP}i_{dgPM} - \omega_e X_{TP} i_{qgPM} - V_{Hdc2}M_{r2}\cos(\alpha_{r2}+\theta_{b2}) \quad (18)$$

where the modulation index M_{ri} of the VSC is used to control the voltage of OWF and the phase angle α_{ri} of the VSC is used to control the active power of OWF.

3) LCC-based Inverter. The per-unit voltage-current equations used to simulate the LCC-based inverter connected to the simplified Taiwan Power System are as follows.

$$(\frac{C_{INV}}{\omega_b})p(V_{qINV}) = i_{qINV} - i_{qgrid} - \omega_r C_{INV} V_{dINV} \quad (19)$$

$$(\frac{C_{INV}}{\omega_b})p(V_{dINV}) = i_{dINV} - i_{dgrid} - \omega_r C_{INV} V_{qINV} \quad (20)$$

$$i_{qINV} = \sqrt{2}\,\frac{I_{HTS}\left(\sqrt{V_{dINV}^4 + V_{dINV}^2V_{qINV}^2 - V_{HTSCC}^2V_{qINV}^2} + V_{HTSCC}V_{qINV}\right)}{V_{dINV}^2 + V_{qINV}^2} \quad (21)$$

$$i_{dINV} = \sqrt{2}\,\frac{I_{HTS}\left(\sqrt{V_{dINV}^2V_{qINV}^2 + V_{qINV}^4 - V_{HTSCC}^2V_{qINV}^2} + V_{HTSCC}V_{dINV}\right)}{V_{dINV}^2 + V_{qINV}^2} \quad (22)$$

$$V_{HTSCC} = \sqrt{(V_{dINV})^2+(V_{qINV})^2}\cos(\gamma_I) - (\frac{\pi}{6})X_{LCI}I_{HTSCC} \quad (23)$$

Fig. 2 shows the control block diagram of the extinction angle of the LCC-based inverter, where the extinction angle is used to control the DC voltage of the hybrid HVDC link.

G. SCESS Model

The SCESS model consists of an SC and a bidirectional DC/DC converter [14]-[16]. The SCESS can regulate the active power of the HVDC link through the bidirectional DC/DC converter operating in either boost or buck mode to deliver active power to the DC link or absorb active power from the DC link of the hybrid HVDC link, respectively.

III. Design of A Damping Controller for the LCC Inverter of the Hybrid HVDC Link

This section presents the design procedure for the damping controller of the LCC-based inverter of the hybrid HVDC link to improve the stability of the studied system using the phase-compensation method based on modal control theory. The nonlinear system equations developed in the previous section are first linearized around a nominal operating point to obtain a set of linearized system dynamic equations as follows.

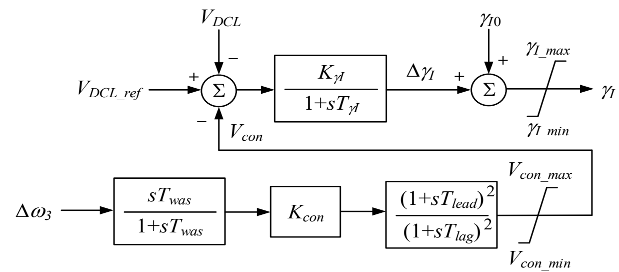

Figure 2. Control block diagram of the extinction angle of the LCC inverter, including the designed lead-lag damping controller.

$$p(\Delta\mathbf{x}) = \mathbf{A}\Delta\mathbf{x} + \mathbf{B}\Delta\mathbf{u} \quad (24)$$

$$\Delta\mathbf{y} = \mathbf{C}\Delta\mathbf{x} \quad (25)$$

where $\Delta\mathbf{x}$ is the state vector, $\Delta\mathbf{u}$ is the input vector, $\Delta\mathbf{y}$ is the output vector, $\mathbf{A}$ is the system matrix, $\mathbf{B}$ is the input matrix, and $\mathbf{C}$ is the output matrix [17]. The control block diagram of the extinction angle of the LCC inverter, including lead-lag damping controller, was shown in Fig. 2, where V_{DCL} is the DC voltage of the hybrid HVDC link, γ_I *is* the extinction angle of the LCC inverter, and $\Delta\omega_3$ is the speed deviation of the SG connected to the bus of Chung-Ho #G. To design the lead-lag damping controller in Fig. 2, the method is based on residue theory [18]-[20]. The transfer function of the damping controller for the LCC-based inverter in Fig. 2 is given by

$$K_{con}H(s) = K_{con}\frac{sT_{was}}{1+sT_{was}}(\frac{1+sT_{lead}}{1+sT_{lag}})^2 \quad (26)$$

where T_{was} is the time constant of the wash-out term and K_{con} is the constant gain. The lead-lag parameter can be determined by using the phase-compensation method in [21-22].

$$\varphi_{con} = 180° - \arg(R_i) \quad (27)$$

$$\alpha_{con} = \frac{T_{lead}}{T_{lag}} = \frac{1-\sin(\varphi_{con}/m_k)}{1+\sin(\varphi_{con}/m_k)} \quad (28)$$

$$T_{lead} = \alpha_{con}T_{lag} \quad (29)$$

$$T_{lag} = 1/\left(\omega_i\sqrt{\alpha_{con}}\right) \quad (30)$$

where φ_{con} is the phase angle of the transfer function $H(s)$, ω_i is the frequency of the poorly damp mode (rad/s), and m_k is the number of compensation stages.

IV. Transient Simulations

This section employs the mathematical models developed in Section II to simulate the transient responses of the studied system when a three-phase short-circuit fault is suddenly applied to bus Jang-Bin H. The applied fault starts at t = 5 s and is cleared at t = 5.1 s while the wind speed of the two OWFs is kept at 11 m/s. Fig. 3 plots the comparative transient responses of the studied system, where the red dashed line, the green dashed line, and the blue solid line represent the responses of the studied system without SCESS, with SCESS

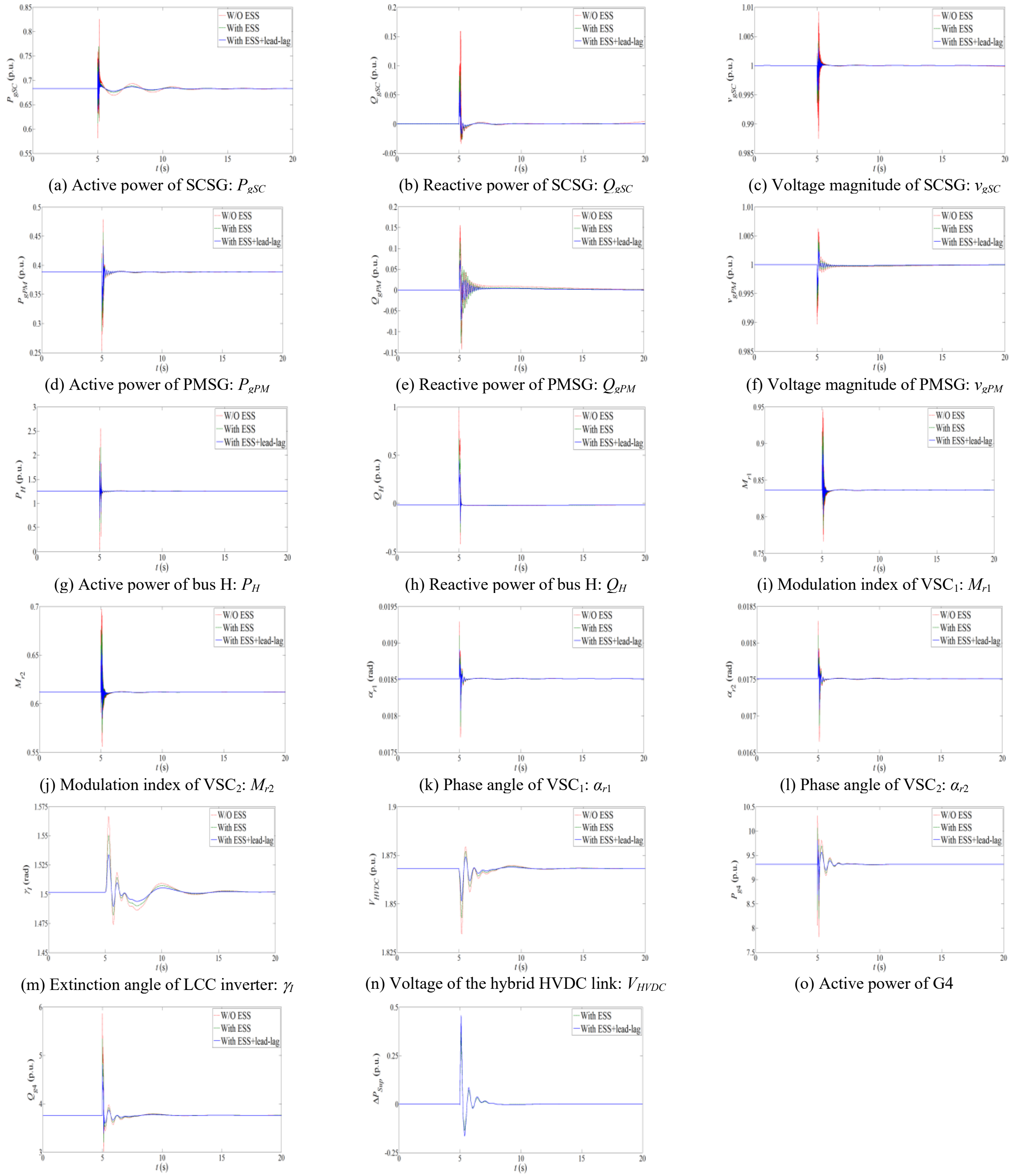

(a) Active power of SCSG: P_{gSC} (b) Reactive power of SCSG: Q_{gSC} (c) Voltage magnitude of SCSG: v_{gSC}

(d) Active power of PMSG: P_{gPM} (e) Reactive power of PMSG: Q_{gPM} (f) Voltage magnitude of PMSG: v_{gPM}

(g) Active power of bus H: P_H (h) Reactive power of bus H: Q_H (i) Modulation index of VSC$_1$: M_{r1}

(j) Modulation index of VSC$_2$: M_{r2} (k) Phase angle of VSC$_1$: α_{r1} (l) Phase angle of VSC$_2$: α_{r2}

(m) Extinction angle of LCC inverter: γ_I (n) Voltage of the hybrid HVDC link: V_{HVDC} (o) Active power of G4

(p) Reactive power of G4 (q) Active power of SCESS

Figure 3. Transient responses of the studied system subject to a three-phase short-circuit fault at the bus of Jang-Bin wind farm H.

but without a damping controller, and with both SCESS and the lead-lag damping controller, respectively.

Figs. 3(a)-3(c) show the comparative transient responses of the active power, reactive power, and voltage magnitude of the SCSG-OWF, respectively. Three responses sag to low values when the fault occurs. After the fault is cleared, these responses can return to the original steady-state operating conditions.

Figs. 3(d)-3(f) plot the comparative transient responses of the active power, reactive power, and voltage magnitude of the PMSG-OWF, respectively. Three responses also sag to low values when the fault occurs. After the fault is cleared,

979-8-3315-8138-1

these responses can also return to the original steady-state operating conditions.

Figs. 3(g) and 3(h) illustrate the comparative transient responses of the active power and reactive power of Jang-Bin bus H injected into the simplified Taiwan Power System, respectively. The active power and reactive power injected into the simplified Taiwan Power System can have the most serious fluctuations when the system is without SCESS. Such transient power fluctuations can be mitigated by the addition of the SCESS connected to the hybrid HVDC link. Furthermore, the smallest power fluctuations can be obtained when the LCC-based inverter with the designed damping controller is in service.

Figs. 3(i)-3(l) plot the comparative transient responses of the modulation index and phase angle of VSC_1 and VSC_2, respectively. Four responses fluctuate when the fault occurs. After the fault is cleared, these responses can return to the original steady-state operating conditions.

Figs. 3(m) and 3(n) show the comparative transient responses of the extinction angle of the LCC inverter and the DC voltage of the hybrid HVDC link, respectively. Two responses fluctuate when the fault occurs. when the fault occurs. After the fault is cleared, these responses can return to the original steady-state operating conditions.

Figs. 3(o) and 3(p) plot the output active power and output reactive power of Hsin-Ta #G, respectively. These results have large transient amplitudes, which are affected by the fault that occurred at the bus of Jang-Bin H. Furthermore, the smallest power fluctuations can be obtained when the LCC inverter with the designed damping controller is in service.

Fig. 3(q) shows the transient responses of the active power of the SCESS. The SCESS can absorb the transmission power of the hybrid HVDC link to avoid too much power being delivered to the simplified Taiwan Power System when the fault occurs.

V. Conclusion

This paper presents the stability improvement of an SCSG-based OWF and a PMSG-based OWF fed into the simplified Taiwan Power System through a hybrid HVDC link with an SCESS and an HTSCC. Transient simulations of the studied system under a three-phase fault at the bus of Jang-Bin H have been conducted. The LCC-based inverter with the designed lead-lag damping controller can improve the performance of the studied system under severe disturbance conditions.

VI. References

[1] T. Nam, J. W. Shim, and K. Hur, “Design and operation of double SMES coils for variable power system through VSC-HVDC connections,” *IEEE Trans. Applied Superconductivity*, vol. 23, no. 3, p. 5701004, Jun. 2013.

[2] T. Nam, J. W. Shim, and K. Hur, “The beneficial role of SMES coil in DC lines as an energy buffer for integrating large scale wind power,” *IEEE Trans. Applied Superconductivity*, vol. 22, no. 3, p. 5701404, Jun. 2012.

[3] L. Qu and W. Qiao, “Constant power control of DFIG wind turbines with supercapacitor energy storage,” *IEEE Trans. Industry Applications*, vol. 47, no. 1, pp. 359-367, Jan./Feb. 2011.

[4] W.-S. Kao, C.-T. Huang, and C.-Y. Chiou, “Dynamic load modeling in Taipower system stability studies,” *IEEE Trans. Power Systems*, vol. 10, no. 2, pp. 907-914, May 1995.

[5] R. E. Torres-Olguin, M. Molinas, and T. Undeland, “Integration of offshore wind farm using a hybrid HVDC transmission composed by the PWM current-source converter and line-commutated converter,” *IEEE Trans. Energy Conversion*, vol. 28, no. 1, pp. 125-134, Mar. 2013.

[6] W. Lin, J. Wen, L. Seca, J. Liang, S. Cheng, M. Yao, and N. Li, “A three-terminal HVDC system to bundle wind farms with conventional power plants,” *IEEE Trans. Power Systems*, vol. 28, no. 3, pp. 2292-2300, Aug. 2013.

[7] J. G. Slootweg and W. L. Kling, “Aggregated modeling of wind parks in power systems,” in *Proc. IEEE Power Tech Conference*, Bologna, Italy, Jun. 23-26, 2003.

[8] G.-H. Kim, N. Kim, K.-M. Kim, M. Park, I.-K. Yu, S. Lee, and T.-J. Park, “EMTDC based simulation of 10 MW class grid-connected superconducting wind turbine generator,” *IEEE Trans. Applied Superconductivity*, vol. 22, no. 3, p. 5202105, Jun. 2012.

[9] N. Kim, G.-H. Kim, K.-M. Kim, M. Park, I.-K. Yu, S. Lee, E. Song, and T.-W. Kim, “Comparative analysis of 10 MW class geared and gearless type superconducting synchronous generators for a wind power generation system,” *IEEE Trans. Applied Superconductivity*, vol. 22, no. 3, p. 5202004, Jun. 2012.

[10] S. M. Osheba, M. A. A. S. Alyan, and Y. H. A. Rahim, “Comparison of transient performance of superconducting and conventional generators in a multimachine system,” *IEEE Trans. Power Apparatus and Systems*, vol. 135, no. 5, pp. 385-396, Sep. 1988.

[11] S. Morimoto, H. Nakayama, M. Sanada, and Y. Takeda, “Sensorless output maximization control for variable-speed wind generation system using IPMSG,” *IEEE Trans. Industry Applications*, vol. 41, no. 1, pp. 60-67, Jan. 2005.

[12] A. Mesemanolis, C. Mademlis, and I. Kioskeridis, “Maximum efficiency of a wind energy conversion system with a PM synchronous generator,” in *Proc. 2010 Power Generation, Transmission, Distribution, and Energy Conversion Conference*, Agia Napa, Cyprus, Nov. 7-10, 2010, pp. 1-9.

[13] P. M. Anderson and A. A. Fouad, *Power System Control and Stability*, Iowa: The Iowa State University Press, Ames, 1977.

[14] N. Mendis, K. M. Muttaqi, and S. Perera, “Management of battery-supercapacitor hybrid energy storage and synchronous condenser for isolated operation of PMSG based variable-speed wind turbine generating systems,” *IEEE Trans. Smart Grid*, vol. 5, no. 2, pp. 944-953, Mar. 2014.

[15] P. K. Ray, S. R. Mohanty, N. Kishor, and A. Mohanty, “Small-signal analysis of hybrid distributed generation system with HVDC-link and energy storage elements,” in *Proc. 2009 2nd International Conference on Emerging Trends in Engineering and Technology*, Nagpur, India, Dec. 16-18, 2009, pp. 1-6.

[16] L. G. Franquelo and J. I. Leon, “How power electronics contribute to the current energy arena,” in *Proc. 2013 7th IEEE GCC Conference and Exhibition*, Doha, Qatar, Nov. 17-20, 2013, pp. 165-171.

[17] L. Wang and D.-N. Troung, “Stability enhancement of DFIG-based offshore wind farm fed to a multi-machine system using a STATCOM,” *IEEE Trans. Power Systems*, vol. 28, no. 3, pp. 2882-2889, Aug. 2013.

[18] A. M. A. Hamdan, “Geometric measures of modal controllability and observability of power system models,” *Electric Power Systems Research*, vol. 15, no. 2, pp. 147-155, Oct. 1988.

[19] J. L. Dominguez-Garcia, F. D. Bianchi, and O. Gomis-Bellmunt, “Control signal selection for damping oscillations with wind power plants based on fundamental limitations,” *IEEE Trans. Power Systems*, vol. 28, no. 4, pp. 4274-4281, Nov. 2013.

[20] A. Heniche and I. Kamwa, “Assessment of two methods to select wide-area signals for power system damping control,” *IEEE Trans. Power Systems*, vol. 23, no. 2, pp. 572-581, May 2008.

[21] Y. Zhang and A. Bose, “Design of wide-area damping controllers for inter-area oscillations,” *IEEE Trans. Power Systems*, vol. 23, no. 3, pp. 1136-1143, Aug. 2008.

[22] N. Yang, Q. Liu, and J. D. McCalley, “TCSC controller design for damping inter-area oscillations,” *IEEE Trans. Power Systems*, vol. 13, no. 4, pp. 1304-1310, Nov. 1998.

979-8-3315-8138-1